A NOVEL ENDMEMBER, FRACTIONAL ABUNDANCE, AND CONTRAST MODEL FOR HYPERSPECTRAL IMAGERY

Scott C. Douglas[1,2]

[1]LGT Corporation
4925 Greenville Ave., Suite 200
Dallas, Texas 75206 USA
Scott.Douglas@lgtcorp.com

[2]Southern Methodist University
Bobby B. Lyle School of Engineering
Dallas, Texas 75275 USA
douglas@lyle.smu.edu

ABSTRACT

In multispectral and hyperspectral image analysis for remote sensing, variations in contrast due to cloud shadows and topography can cause problems in the demixing process, creating false endmembers and erroneous fractional abundance images. This paper introduces a novel hyperspectral mixing model in which pixel contrast is accounted for explicitly in the image formation. A method is described for estimating the per-pixel contrast for any chosen endmember-based demixing algorithm. Applications of the method to both synthetic and real-world satellite imagery illustrate its efficacy.

***Index Terms*—** Hyperspectral imaging, multispectral imaging, image color analysis, remote sensing, geophysics

1. INTRODUCTION

Remotely-sensed electro-optical imagery is widely-used in a number of fields, including geology and geophysics, defense and security, and the environmental sciences [1]–[5]. By analyzing the mathematical structure of the image pixels, various features of the observed area can be analyzed, such as surface minerology, geological structure including faulting and folding, the effects of natural processes, and man-made changes.

Since the advent of persistent multispectral and hyperspectral imagers on satellite platforms, there has been ongoing interest in the automated analysis of sensed imagery that takes into account all possible non-idealities of the image formation process. One of these effects is the variation in pixel contrast due to either (a) shadowing caused by clouds or (b) topographical variations. Cloud cover obscures regions in the line of sight of the image sensor, but it also decreases the contrast of regions in the line of illumination. A de-shadowing method has been developed [6], but it requires some manual adjustment to work properly. Topographical variations cause differences in reflectance due to changes in the angle of reflection and are typically corrected for using digital elevation and the angular position of the Sun at the time the image is collected. This process complicates the analysis procedure, is often done manually, and does not scale well to large images. It also requires the alignment and merging of two different data sets – assuming that the elevation data is available – thus compounding errors. Such errors can hamper the analysis if a blind endmember-based demixing approach is used to perform the image decomposition. Most methods for hyperspectral image analysis proposed in the scientific literature employ a blind endmember-finding or simplex approach [7]–[16].

In this paper, a novel model for multispectral and hyperspectral image formation is described. This model allows for *changes in contrast* on a per-pixel basis, thus potentially-overcoming analysis issues associated with topographical variations and shadowing. Using this model, we show how standard endmember-finding methods can be applied to per-pixel normalized hyperspectral images, generating normalized fractional abundance images and endmember spectra. We provide a procedure for relating these normalized quantities to those of the standard model, from which errors in estimation due to contrast variations can be gauged. The approach has an additional practical benefit: When applied to images with significant contrast variations, it prevents the generation of "false" endmembers and abundance images caused by shadowing and topographical variations, preserving precious endmember dimensions for more-significant image features, and leading to higher-quality image analysis.

2. THE ENDMEMBER - FRACTIONAL ABUNDANCE - CONTRAST MODEL

Let a hyperspectral pixel s_λ at a particular wavelength λ and position (x, y) be defined as

$$s_\lambda(x,y) \;=\; \sum_{p=1}^{M} \overline{m}_{\lambda,p}\overline{\alpha}_p(x,y)\gamma(x,y), \qquad (1)$$

where $\overline{m}_{\lambda,p}$ is the pth normalized endmember response at wavelength λ across the entire scene for $1 \leq p \leq M$, $\overline{\alpha}_p(x,y)$ is the normalized fractional abundance of the pth material at position (x, y), and $\gamma(x, y)$ is the contrast of the pixel at position (x, y). We differentiate contrast $\gamma(x, y)$ from scattering. Scattering could be different for different materials and is indexed by the particular endmember, whereas contrast is constant across the endmembers for a given position in this model. In this model, we impose the following two constraints:

$$\sum_{p=1}^{M} \overline{\alpha}_p(x,y) = 1, \qquad \sum_{\lambda=1}^{L} \overline{m}_{\lambda,p} = 1, \tag{2}$$

where M and L are the number of discrete endmembers and wavelength measurements per spectral response, respectively. The first constraint is standard for fractional abundances and carries over to this new model. The second constraint is new and implies that the "gain" in each endmember is constant; *i.e.* the area under each endmember spectral curve sums to one.

This model differs from that typically used in hyperspectral image processing, in which the image is first calibrated to try to remove any variations in contrast, yielding the model

$$s_\lambda(x,y) \quad = \quad \sum_{p=1}^{M} m_{\lambda,p}\alpha_p(x,y) \tag{3}$$

where no scattering or contrast variation is assumed. In this standard model, $m_{\lambda,p}$ is the pth endmember response at wavelength λ across the entire scene, and $\alpha_p(x,y)$ is the fractional abundance of the pth material at position (x,y), In the standard model, a sum-to-one constraint on the abundances is imposed:

$$\sum_{p=1}^{M} \alpha_p(x,y) \quad = \quad 1. \tag{4}$$

There are no constraints placed on the endmember responses $m_{\lambda,p}$ nor the pixels $s_\lambda(x,y)$ other than their positivity.

We now relate the two models. To do so, consider the sum of the hyperspectral pixels in wavelength space:

$$\begin{aligned}
\sum_{\lambda=1}^{L} s_\lambda(x,y) &= \sum_{\lambda=1}^{L}\sum_{p=1}^{M} \overline{m}_{\lambda,p}\overline{\alpha}_p(x,y)\gamma(x,y) && (5)\\
&= \sum_{p=1}^{M}\left(\sum_{\lambda=1}^{L} \overline{m}_{\lambda,p}\right)\overline{\alpha}_p(x,y)\gamma(x,y) && (6)\\
&= \gamma(x,y)\sum_{p=1}^{M}\overline{\alpha}_p(x,y) && (7)\\
&= \gamma(x,y). && (8)
\end{aligned}$$

In the above relations, we have used the constraints on $\overline{\alpha}_p(x,y)$ and $\overline{m}_{\lambda,p}$ to simplify the relations. We can see now that $\gamma(x,y)$ is well-described by the term contrast, as it represents the area under the wavelength curve of the hyperspectral pixel $s_\lambda(x,y)$. Moreover, if we define the normalized hyperspectral pixel

$$\overline{s}_\lambda(x,y) \quad = \quad \frac{s_\lambda(x,y)}{\gamma(x,y)}, \tag{9}$$

it is straightforward to show that

$$\overline{s}_\lambda(x,y) \quad = \quad \sum_{p=1}^{M} \overline{m}_{\lambda,p}\overline{\alpha}_p(x,y), \tag{10}$$

where the following additional constraint is imposed along with those in (2):

$$\sum_{\lambda=1}^{L} \overline{s}_\lambda(x,y) \quad = \quad 1. \tag{11}$$

Clearly, normalized fractional abundances are nonlinearly-related to fractional abundances, with the degree of nonlinearity dependent on the variations in the energies of the endmembers. Fractional abundances for which endmembers are "bright" have higher normalized fractional abundances.

The implications of the above relations are the following:

1. Normalizing each hyperspectral pixel to unit gain has the implication that the normalized endmembers being found have unit gain.

2. The normalized hyperspectral model has different abundances from the regular hyperspectral model. If we equate

$$\begin{aligned}
\sum_{p=1}^{M} \overline{m}_{\lambda,p}\gamma(x,y)\overline{\alpha}_p(x,y) &= \sum_{p=1}^{M} m_{\lambda,p}\alpha_p(x,y) && (12)\\
&= \sum_{p=1}^{M} \overline{m}_{\lambda,p}\sum_{l=1}^{L} m_{l,p}\alpha_p(x,y) && (13)
\end{aligned}$$

such that

$$\overline{\alpha}_p(x,y) \quad = \quad \alpha_p(x,y)\frac{\sum_{l=1}^{L} m_{l,p}}{\sum_{q=1}^{M}\sum_{\lambda=1}^{L} m_{\lambda,q}\alpha_q(x,y)} \tag{14}$$

we see that $\overline{\alpha}_p(x,y)$ differs from $\alpha_p(x,y)$ in a complicated fashion. Moreover, while normalization of hyperspectral imagery prior to endmember identification has previously been deemed useful – see *e.g.* [7] – the implications of the relation in (14) appear to be largely unexplored.

3. ESTIMATING THE MODEL PARAMETERS

The new model introduced in this paper has a distinct advantage over the traditional endmember model: Pixel contrast variations are explicitly accounted for in the new model. Thus, data for which pixel contrast $\gamma(x,y)$ varies over the scene will be better handled by the new model. By using the normalized pixels $\overline{s}_\lambda(x,y)$, we can effectively cancel out pixel contrast, and all other rules regarding endmember estimation still hold, including positivity of $\overline{m}_{\lambda,p}$ and the sum-to-one nature of the normalized fractional abundances $\overline{\alpha}_p(x,y)$. These normalized quantities, however, are incorrect from the point of view of the standard model.

In this section, we show how to relate the parameters of the new normalized model to those of the standard model. Through these relationships, we can determine the *amount of error* in the standard model, resulting in a measure of degree of fit to the standard model that has heretofore been unavailable.

To relate $\{\overline{m}_{\lambda,p}, \overline{\alpha}_p(x,y), \gamma(x,y)\}$ to $\{m_{\lambda,p}, \alpha_p(x,y)\}$,

$$\gamma(x,y)\overline{\alpha}_p(x,y) \quad = \quad \alpha_p(x,y)\sum_{l=1}^{L} m_{l,p}. \tag{15}$$

Assume that we have used endmember estimation in normalized pixel space to estimate $\{\overline{\alpha}_p(x,y)\}$, and note that $\gamma(x,y)$ is calculated from the received pixels. The terms on the right of this equation are unknown. Define the quantity

$$c_p \quad = \quad \frac{1}{\sum_{l=1}^{L} m_{l,p}}. \tag{16}$$

Then, we have

$$\gamma(x,y)\overline{\alpha}_p(x,y)c_p \quad = \quad \alpha_p(x,y). \tag{17}$$

Taking the sum of both sides of the above equation over p,

$$\gamma(x,y)\sum_{p=1}^{M}\overline{\alpha}_p(x,y)c_p \quad = \quad 1. \tag{18}$$

This relationship is a constraint that holds for all pixel positions (x,y). Define

$$\mathbf{A} = \begin{bmatrix} \gamma(x_1,y_1)\alpha_1(x_1,y_1) & \cdots & \gamma(x_1,y_1)\alpha_M(x_1,y_1) \\ \vdots & & \vdots \\ \gamma(x_N,y_N)\alpha_1(x_N,y_N) & \cdots & \gamma(x_N,y_N)\alpha_M(x_N,y_N) \end{bmatrix} \tag{19}$$

$$\mathbf{c} \quad = \quad [c_1 \cdots c_M]^T, \tag{20}$$

where we have assumed the image to have N spatial positions (x_1,y_1) to (x_N,y_N). Then, we have

$$\mathbf{Ac} \quad = \quad \mathbf{1}, \tag{21}$$

where $\mathbf{1}$ is an N-dimensional vector of ones. The solution to this equation is

$$\mathbf{c} \quad = \quad (\mathbf{A}^T\mathbf{A})^{-1}\mathbf{A}^T\mathbf{1}. \tag{22}$$

Once $\mathbf{c}$ is known, it is straightforward to show that

$$m_{\lambda,p} \quad = \quad \frac{\overline{m}_{\lambda,p}}{c_p} \tag{23}$$

$$\widehat{\alpha}_p(x,y) \quad = \quad c_p\gamma(x,y)\overline{\alpha}_p(x,y). \tag{24}$$

where $\widehat{\alpha}_p(x,y)$ is the estimate of $\alpha_p(x,y)$ under our variable-contrast model.

Thus, the procedure for estimating the endmembers and abundances is as follows:

Step #1: Normalize the hyperspectral image pixels $s_\lambda(x,y)$ to obtain $\overline{s}_\lambda(x,y)$ using Eqns. (8) and (9).

Step #2: Apply any endmember extraction scheme to the normalized pixels to obtain $\{\overline{m}_{\lambda,p}\}$ and $\{\overline{\alpha}_p(x,y)\}$.

Step #3: Use Eqn. (22) to compute the corrections $\{c_p\}$.

Step #4: Compute the endmembers and fractional abundances using Eqns. (23) and (24).

4. SYNTHETIC EXAMPLE

The following synthetic example shows the efficacy of the above relations. It also shows how we can test the correctness of the conventional hyperspectral mixing model in (3) in relation to the generalized model in (1) in which we set

$$\gamma(x,y) \quad = \quad 1 + \Delta\gamma(x,y), \tag{25}$$

where $\Delta\gamma(x,y)$ accounts for small per-pixel contrast variations. We first generate $M = 3$ random Unif[0,1] fractional abundance images of size 40×40 pixels. We then generate a synthetic mixture of $L = 9$ hyperspectral bands from these images according to the generalized mixture model given by (25), where we have selected certain pixels to have a 1% higher contrast, or $\Delta\gamma(x,y) = 0.01$. Random uncorrelated Guassian noise with standard deviation of 0.001 has been added to each pixel. The left side of Fig. 1 shows these nine image bands. We normalize the nine-band pixels, apply the vertex component analysis (VCA) algorithm [8] to this data, and then use our correction method to compute the endmembers and fractional abundances. The resulting images are estimated with an average SNR of 18.8dB in permuted order. Performing the same calculations with the unnormalized image data with the standard approach yields an average SNR of only 15.9dB. This shows that the proposed method can estimate fractional abundances with a higher quality than the standard approach when contrast variations are present.

Fig. 1(a) shows the contrast variation that we have imposed on the pixels, corresponding to the image $\Delta\gamma(x,y)$. Fig. 1(b) shows the average contrast of the nine hyperspectral bands, in which the contrast information is difficult to discern. Fig. 1(c) shows the average contrast of the normalized fractional abundances,

$$\overline{\gamma}(x,y) \quad = \quad \sum_{p=1}^{M}\overline{\alpha}_p(x,y). \tag{26}$$

No discernable structure is apparent, as contrast has been properly accounted for by our process at this stage. Fig. 1(d) shows the average contrast of the estimated fractional abundances, given by

$$\widehat{\gamma}(x,y) \quad = \quad \sum_{p=1}^{M}\widehat{\alpha}_p(x,y), \tag{27}$$

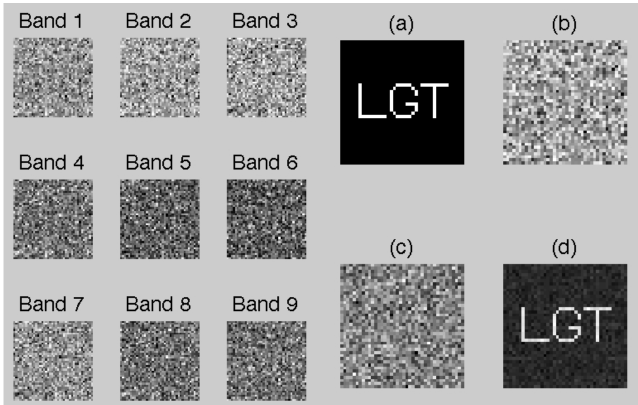

Fig. 1. Synthetic example; see text for explanation.

where we have scaled the image to emphasize the contrast variations. As can be seen, the contrast information is discernable after our process in the standard abundance model. This shows that we can identify variations in per-pixel contrast using our method.

5. REMOTE SENSING EXAMPLE

We now explore the proposed method in a remote sensing example. Fig. 2 shows the infrared Band 3N of a 4.5km $\times$ 4.5km portion of an ASTER [17] image scene over southern Kentucky with a pixel size of 15m. This multispectral image has three prominent clouds – one located near the center, and two located to the north – that cast shadows to the northwest of their position as viewed from the satellite sensor. It also shows variations in contrast due to changes in topography, in which there are rolling hills that trend northeast-to-southwest. We process this image using the same procedure as described in the synthetic example above, with the following parameters: $L = 9$ corresponding to the three VNIR and six SWIR bands of the ASTER data, and $M = 7$ endmembers.

Fig. 3 shows the resulting abundance images produced by both the standard processing (left) and our proposed processing (right) for two different identified spatial features in the data. In this image, "hot" colors correspond to high abundance, whereas "cool" colors correspond to low abundance. The upper two images show the fractional abundances corresponding to grass clearings for each of the methods. As can be seen, the abundance image produced by our proposed approach on the upper right more clearly delineates these regions, with more well-defined high-abundance shapes, as compared to that produced by the standard approach.

The lower two-images in Fig. 3 are the result of the contrast variations due to both cloud shadows and topographical changes and represent artifacts in the endmember identification process. The standard approach identifies the cloud shadow regions as "high abundance", and incorrectly associates portions of the rolling hills to this identified endmember. Our proposed approach produces an artifact image with a much weaker response, and the hilly portions of the scene are not associated with the cloud shadows.

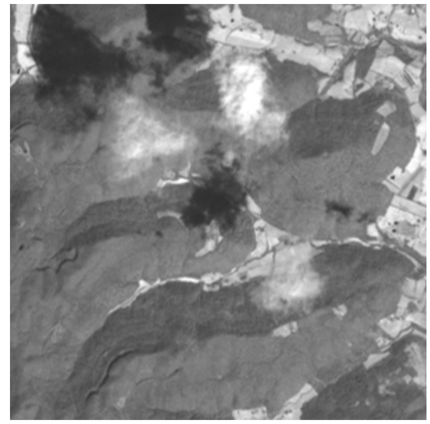

Fig. 2. Infrared Band 3N of ASTER Scene

6. CONCLUSIONS

In this paper, we describe a novel hyperspectral image model in which per-pixel contrast values are parameters to be identified. The model leverages existing endmember-based demixing algorithms applied to normalized spectral responses and corrects for the resulting abundance values after demixing. Application of the approach to both synthetic and real-world remote sensing images shows that the procedure identifies abundance images more accurately and generates fewer artifacts than the standard approach. Note that our procedure imposes a normalized endmember constraint in the demixing process, and it is unclear how this constraint affects the accuracy of endmember identification when endmembers have similar shapes but different magnitudes [18]. This issue is the subject of current study.

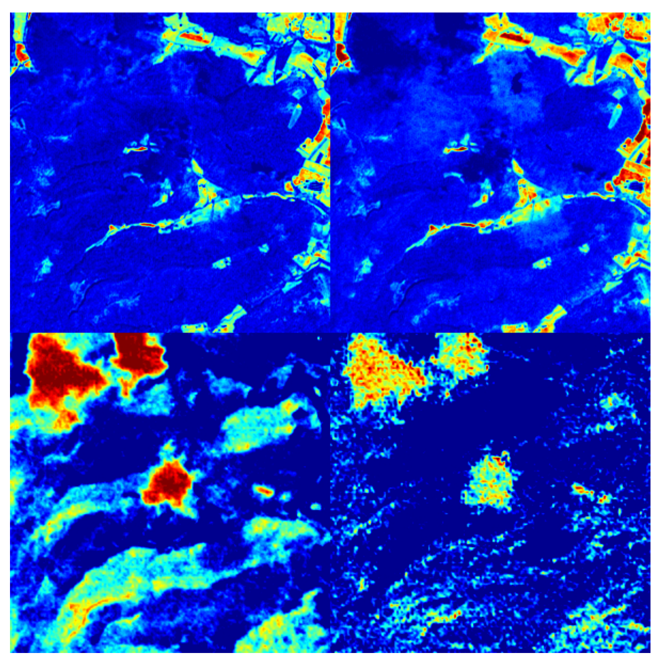

Fig. 3. Four images showing fractional abundances produced by the various methods; see text for explanation.

7. REFERENCES

[1] F.D. van der Meer, H.M.A. van der Werff, F.J.A. van Ruitenbeek, C.A. Hecker, W.H. Bakker, M.F. Noomen, M. van der Meijde, E.J.M. Carranza, J.B. Smeth, and T. Woldai, "Multi- and hyperspectral geologic remote sensing: A review," *International Journal of Applied Earth Observation and Geoinformation.,* volume 14, number 1, pages 112-128, February 2012.

[2] D. Gillis, J. Bowles, and M. E. Winter, "Using endmembers as a coordinate system in hyperspectral imagery." *Proceedings of the SPIE Symposium on Imaging Spectrometry VIII,* Orlando, FL, November 2002.

[3] C.-I. Chang, *Hyperspectral Imaging: Techniques for Spectral Detection and Classification,* (New York: Kluwer, 2003).

[4] D.G. Goodenough, A. Dyk, K.O. Niemann, J.S. Pearlman, H. Chen, T. Han, M. Murdoch, and C. West, "Processing Hyperion and ALI for forest classication," *IEEE Transactions on Geoscience and Remote Sensing,* volume 41, pages 1321-1331, June 2003.

[5] J. Zhang, K. Staenz, P. Eddy, N. Rochdi, D. Rolfson, and A. Smith, "Analysis of spaceborne Hyperion imagery for the estimation of fractional cover of rangeland ecosystems," *International Archives of Photogrammetry, Remote Sensing, and Spatial Information Sciences,* volume 37, part B7, 2008.

[6] S.M. Adler-Golden, M.W. Matthew, G.P. Anderson, G.W. Felde, and J.A. Gardner, "An algorithm for deshadowing spectral imagery," *Proceedings of the SPIE Symposium on Imaging Spectrometry VIII,* Orlando, FL, November 2002.

[7] M. Berman, H. Kiiveri, P. Lagerstrom, A.T. Ernst, R. Dunne, and J.F. Huntington, "ICE: a statistical approach to identifying endmembers in hyperspectral images," *IEEE Transactions on Geoscience and Remote Sensing,* volume 42, number 10, pages 2085-2095, October 2004.

[8] J.M.P. Nascimento and J.M. Bioucas-Dias, "Vertex component analysis: A fast algorithm to unmix hyperspectral data," *IEEE Transactions on Geoscience and Remote Sensing,* volume 43, number 4, pages 898-910, April 2005.

[9] C.-I. Chang and A. Plaza, "A fast iterative algorithm for implementation of pixel purity index," *IEEE Geoscience and Remote Sensing Letters,* volume 3, number 1, pages 63-67, January 2006.

[10] A. Zare and P. Gader, "Sparsity promoting iterated constrained endmember detection for hyperspectral imagery," *IEEE Geoscience and Remote Sensing Letters,* volume 4, number 3, pages 446–450, July 2007.

[11] J. Li and J.M. Bioucas-Dias, "Minimum volume simplex analysis: A fast algorithm to unmix hyperspectral data," *Proceedings of the IEEE International Geoscience and Remote Sensing Symposium,* Boston, MA, volume 3, pages 250-253, July 2008.

[12] A.M. Filippi and R. Archibald, "Support vector machine-based endmember extraction," *IEEE Transactions on Geoscience and Remote Sensing,* volume 47, number 3, pages 771-791, March 2009.

[13] B. Luo, J. Chanussot, S. Doute, and X. Ceamanos, "Unsupervised endmember extraction of Martian hyperspectral images," *Proceedings of the 1st Workshop on Hyperspectral Image and Signal Processing: Evolution in Remote Sensing,* Grenoble, France, paper 131, pages 1-4, August 2009.

[14] N. Dobigeon, S. Moussaoui, M. Coulon, J.-Y. Tourneret, and A. O. Hero, "Joint Bayesian endmember extraction and linear unmixing for hyperspectral imagery," *IEEE Transactions on Signal Processing,* volume 57, pages 4355-4368, November 2009.

[15] T.-H. Chan, J.-Y. Liou, A. Ambikapathi, W.-K. Ma, and C.-Y. Chi, " Fast algorithms for robust hyperspectral endmember extraction based on worst-case simplex volume maximization," *Proceedings of the IEEE International Conference on Acoustics, Speech, and Signal Processing,* Kyoto, Japan, pages 1237-1240, March 2012.

[16] J. M. Bioucas-Dias, A. Plaza, N. Dobigen, M. Parente, Q. Du, and P. Gader, "Hyperspectral unmixing overview: Geometrical, statistical and sparse regression-based approaches," *IEEE Journal of Selected Topics in Applied Earth Observations and Remote Sensing,* volume 5, pages 354-379, April 2012.

[17] Y. Yamaguchi, A.B.Kahle, H. Tsu, T. Kawakami, and M. Pniel, "Overview of Advanced Spaceborne Thermal Emission and Reflection Radiometer (ASTER)," *IEEE Transactions on Geoscience and Remote Sensing,* volume 36, number 4, pages 1062-1071, July 1998.

[18] J.N. Sweet, "The spectral similarity scale and its application to the classification of hyperspectral remote sensing data," *Proceedings of the IEEE Workshop on Advances in Techniques for Analysis of Remotely-Sensed Data,* pages 92-99, October 2003.